ACCSCIENCE PUBLISHING
An International Journal of Optimization and Control: Theories & Applications
ISSN: 2146-0957 eISSN: 2146-5703
Vol. 16, No. 3, pp.1109-1125 (2026)
https://doi.org/10.36922/IJOCTA026050018
IJOCTA
RESEARCH ARTICLE

Comparison of robust, optimal, and lightweight learning-based controllers for frequency and voltage regulation in inverter-dominated microgrids

Minh-Cuong Nguyen[1,2*]

[1] Education Technology and Adaptive Learning Institute, Thai Nguyen University of Technology, Thai Nguyen, Vietnam
[2] Faculty of Electrical Engineering, Thai Nguyen University of Technology, Thai Nguyen, Vietnam
nmc.etali@tnut.edu.vn

ARTICLE INFO

Article history:
Received: January 29, 2026
Revised: March 30, 2026
Accepted: April 7, 2026
Published Online: May 22, 2026

Keywords:
Microgrid control
Frequency regulation
Voltage regulation
Robust control
Lightweight machine learning

AMS Classification 2010:
90B50, 90C90

ABSTRACT

In inverter-dominated microgrids with high renewable penetration, frequency and voltage regulation are strongly affected by load steps, source variability, and reduced inertia, which raises the question of how different control strategies trade off tracking accuracy, dynamic stress, power quality, and control effort under identical operating conditions. We conducted a systematic and reproducible comparison of six representative controllers, including active disturbance rejection control, sliding mode control, model predictive control, fuzzy proportional–integral–derivative control, and two lightweight learning-assisted approaches based on extreme learning machines and least-squares support vector machines. All controllers were evaluated on the same control-oriented microgrid model using stochastic renewable profiles, step load disturbances, measurement noise, and multiple Monte Carlo realizations. Performance was assessed using quantitative metrics covering frequency tracking, transient response, rate of change of frequency, voltage deviation, harmonic distortion, and control activity. The results show that fuzzy proportional–integral–derivative control achieved the best overall tracking performance with a root mean square error of 0.00753 Hz and an integral absolute error of 0.05586 Hz, while maintaining a moderate control effort of 0.200 p.u. Sliding mode control yielded the lowest voltage total harmonic distortion at 3.30%, whereas model predictive control produced the smoothest control signal with a mean control effort of 0.017 p.u., but it suffers from significantly larger tracking errors, with a root mean square error of 0.07488 Hz. These results demonstrate that controller performance is strongly metric-dependent and that no single strategy is universally optimal for all operational objectives.

1. Introduction

The rapid increase in renewable energy sources (RES) interfaced through power converters—together with the trend of microgrids operating under an inverter-dominated architecture—is changing the nature of the frequency and voltage control problem toward increased sensitivity to load disturbances, source variability, and parameter uncertainties. In this study, the term microgrid refers to a small-scale electrical distribution system that integrates distributed generation units, energy storage, and local loads, and is capable of operating either in grid-connected mode or autonomously in an islanded mode, independently of the main utility grid. In that context,

* Corresponding Author

grid-forming control has become an important technical pillar for maintaining synchronization, sharing power, and ensuring power quality in both islanded and interconnected modes while still respecting converter hardware constraints and current limits[1,2] Recent studies demonstrate that the range of grid-forming solutions is broad, from droop and virtual synchronous generators to variants based on oscillators and optimal control, yet the gap between research findings and practical deployment conditions remains significant due to differences in modeling assumptions, test scenarios, and evaluation criteria.[3] At the same time, system-level analyses emphasize that as the share of converter-interfaced sources increases, traditional stability mechanisms based on mechanical inertia are no longer inherently available, making the requirements for local and coordinated control more stringent, especially under fast disturbances and constant-power-type load variations.[4–6]

From a dynamic perspective, recent studies indicate that the reduction of effective inertia and control interactions among multiple converters can increase the risk of frequency oscillations, raise the rate of change of frequency (ROCOF), and weaken small-signal stability margins, particularly when the microgrid experiences step load events and rapidly changing operating conditions.[7,8] Beyond stability requirements and transient response, constraints on current limits and behavior under symmetrical faults have also become decisive factors for deployment feasibility, because grid-forming control strategies often need to reconcile voltage waveform preservation, current limiting, and synchronization maintenance.[9–11] These aspects are further shaped by evolving interconnection expectations and protection requirements in inverter-dominated systems.[12] Therefore, a control strategy regarded as practically suitable needs not only to achieve tracking quality and reduce oscillations, but also to maintain safety margins under strong disturbances, while also ensuring that computational requirements remain compatible with real-time implementation.

In robust control approaches, methods such as active disturbance rejection control (ADRC) and linearized disturbance-observer–based designs have attracted attention due to their ability to aggregate uncertainties and disturbances into a compensation channel, thereby reducing dependence on an accurate model and increasing tolerance to parameter variations.[13–15] In parallel, sliding mode control (SMC) methods and finite-time variants provide fast convergence mechanisms and formal robustness properties, fitting contexts with strong disturbances and constrained control signals, although caution is always needed regarding chattering and the actual bandwidth limits of hardware.[16–18] These robust methods often have advantages in implementation simplicity and reliability under uncertainty, but may face limitations when simultaneous optimization of multiple criteria is required or when current constraints and saturation strongly dominate the dynamics.

In constraint-based optimization approaches, model predictive control (MPC) and predictive variants for converters provide a natural framework for handling control limits, state constraints, and multi-objective criteria, thereby improving frequency and voltage responses under load disturbances and source variability.[19,20] Nevertheless, classical MPC often faces computational burdens and sensitivity to model errors, especially when the microgrid has a complex structure or when LCL parameters and loads vary over time.[21] Accordingly, recent developments have focused on adaptive MPC, model-free prediction, and data-driven uncertainty compensation mechanisms to reduce model dependence and increase real-time feasibility.[22–24]

On the other hand, several studies of frequency control in systems with a high share of converter-interfaced sources show that the methodological landscape is fragmented by scenario and scale, making conclusions about superiority among method classes sometimes dependent on specific simulation setups.[25] This has motivated broader comparative discussions that stress consistency in scenarios, metrics, and implementation assumptions.[26,27] Grid-forming approaches based on oscillator control and distributed synchronization also show potential for hierarchical characteristics and multi-converter coordination capability, but results are often sensitive to network assumptions, communication delays, and measurement noise.[28–30] This highlights the need for a systematic comparative evaluation, in which representative algorithms are placed under the same scenario conditions, the same control limits, and the same set of technical criteria.

At the microgrid level, nonlinearity due to constant power loads and multi-converter interactions often exposes differences among strategies in stability margins and robustness when operating far from the nominal point; thus, valuable conclusions need to consider multiple scenarios and assess ranking stability under noise and uncertainty.[31,32] Such effects are also shaped by controller structure and the way disturbance and uncertainty enter the closed-loop system.[33] At the

same time, data-driven directions in microgrid operation, such as short-term forecasting and energy management optimization, suggest a practical role for lightweight machine learning (ML) models in supporting control, such as parameter adjustment by operating states, fast approximation of control laws, or inference of disturbances and uncertainties from measured signals.[34–36] This approach is particularly suitable when the goal is to improve control quality while maintaining low computational cost.

Based on these observations, this study aims at a systematic comparative evaluation in the spirit of controlled experimental conditions, rather than making a generic statement applicable to all systems. On a unified simulation platform, representative control variants are placed under the same load disturbance scenarios, source variability, and measurement noise, together with saturation limits and current limits to reflect practical deployment conditions.[25] Specifically, the study proposes a comparative evaluation protocol and a multi-criteria technical metric set for frequency and voltage, including tracking, transient response, ROCOF, oscillations, control effort, and scenario sensitivity.[37,38] In addition to robust and constraint-based optimization classes, the study also examines the role of lightweight ML in assisting control and operating-state–dependent decision making, in a practical direction with risk control.[39] Above all, the selection of metrics and the way results are aggregated are tied to concepts of virtual inertia, oscillation attenuation, and stability margins observed in modern microgrids to ensure technically meaningful interpretation.[40]

2. System modeling and problem formulation

Consider an inverter-dominated AC microgrid consisting of Nvoltage-source converters operating under a grid-forming strategy, interconnected through a distribution network represented by the nodal admittance matrix $\mathbf{Y}_{\text{bus}} \in \mathbb{C}^{N\times N}$, together with RES sources and loads at the nodes. Recent studies indicate that control-oriented modeling is necessary to balance dynamic fidelity and computational feasibility, particularly when the objective is to fairly compare different control strategies under the same disturbance scenarios and consistent hardware constraints.[41]

To clarify the dynamics that directly govern frequency and voltage tracking performance, an averaged model in the synchronous dq reference frame aligned with the internal phase of each inverter is employed. For the inverter i, the main state variables include the filter inductor current ($\mathbf{i}_{f,i}$), the filter capacitor voltage ($\mathbf{v}_{c,i}$), the grid-side current ($\mathbf{i}_{g,i}$), the internal frequency (ω_i), and the internal phase (θ_i). A low-order LCL (inductor–capacitor–inductor) filter model in a control-oriented form is considered sufficient to capture the dominant interactions between the inverter and the grid in comparative control studies.[13]

The dynamics of the inverter-side inductor are described in **Equation 1**:

$$L_f\dot{\mathbf{i}}_{f,i} = -R_f\mathbf{i}_{f,i} + \mathbf{v}_{\text{inv},i} - \mathbf{v}_{c,i} + \omega_i\mathbf{J}L_f\mathbf{i}_{f,i} \quad (1)$$

where $L_f, R_f$are the filter parameters, $\mathbf{v}_{\text{inv},i}$ is the equivalent modulated voltage, and $\mathbf{J}$ is the rotation operator in the dqframe.

The filter capacitor dynamics are described as in **Equation 2**:

$$C_f\dot{\mathbf{v}}_{c,i} = \mathbf{i}_{f,i} - \mathbf{i}_{g,i} + \omega_i\mathbf{J}C_f\mathbf{v}_{c,i} \quad (2)$$

For the grid-coupling branch, the inductor dynamics are expressed by **Equation 3**.

$$L_g\dot{\mathbf{i}}_{g,i} = -R_g\mathbf{i}_{g,i} + \mathbf{v}_{c,i} - \mathbf{v}_{b,i} + \omega_i\mathbf{J}L_g\mathbf{i}_{g,i} \quad (3)$$

To describe multi-node interactions, a complex representation $\tilde{v}_i = v_{d,i} + \mathrm{j}v_{q,i}$and $\tilde{i}_{g,i} = i_{d,i} + \mathrm{j}i_{q,i}$are used. The nodal relationship is then written as in **Equation 4**.

$$\tilde{\mathbf{i}}_g = \mathbf{Y}_{\text{bus}}\tilde{\mathbf{v}}_b + \tilde{\mathbf{i}}_L - \tilde{\mathbf{i}}_{\text{RES}} \quad (4)$$

This representation forms the basis for stability and control studies of microgrids based on nodal modeling[42].

The load at each node is modeled using a ZIP structure with a constant power component to reflect nonlinearity and negative impedance effects in practical operation. The load model is written as in **Equation 5**:

$$\begin{aligned}\tilde{i}_{L,i} &= (G_{Z,i} + \mathrm{j}B_{Z,i})\,\tilde{v}_i \\ &+ \tilde{i}_{I,i} + \tfrac{P_{P,i} - \mathrm{j}Q_{P,i}}{\tilde{v}_i^*} + \tilde{d}_{L,i}\,(t)\end{aligned} \quad (5)$$

where the constant power component is known to reduce stability margins and increase the sensitivity of microgrids to fast load disturbances.[43]

The internal frequency dynamics of a grid-forming inverter are described by a virtual inertia model as in **Equation 6**. This model encompasses the modern virtual synchronous machine and droop variants and is widely used in microgrid stability and control analysis.[23]

$$2H_i\dot{\omega}_i = P_i^\star - P_i - D_i\,(\omega_i - \omega_{\text{nom}}) + d_{\omega,i}\,(t) \quad (6)$$

Similarly, the voltage magnitude dynamics are described as in **Equation 7**:

$$\tau_{E,i}\dot{E}_i = E_i^\star - E_i - k_{Q,i}\,(Q_i - Q_i^\star) + d_{E,i}\,(t) \quad (7)$$

The power at the point of common coupling is determined from the *dq*quantities as in **Equation 8**. The internal phase of the inverter is updated according to **Equation 9**. The voltage reference in the *dq* frame is defined as in **Equation 10**.

$$P_i + \mathrm{j}Q_i = \tilde{v}_i \tilde{i}^*_{g,i} \tag{8}$$

$$\dot{\theta}_i = \omega_i \tag{9}$$

$$\mathbf{v}^{\mathrm{ref}}_{c,i} = E_i \begin{bmatrix} \cos\theta_i \\ \sin\theta_i \end{bmatrix} \tag{10}$$

Hardware constraints are incorporated through modulation voltage limits and current limits. The modulation voltage constraint is written as in **Equation 11**, while the current limits are described by **Equation 12**, where $\mathbf{v}_{\mathrm{inv},i}, \mathbf{i}_{f,i}$, and $\mathbf{i}_{g,i}$ denote the inverter output-voltage vector, filter-inductor current vector, and grid-side current vector of the $i-th$ inverter, respectively; $V_{\mathrm{dc},i}$ is the DC-link voltage, κ_v is the modulation-dependent voltage limit coefficient, $I_{i,\max}$ is the maximum allowable current, and $\cdot_2$ denotes the Euclidean norm representing the resultant magnitude of the corresponding vector in the *dq* frame.

$$\| \mathbf{v}_{\mathrm{inv},i} \|_2 \leq \kappa_v V_{\mathrm{dc},i} \tag{11}$$

$$\| \mathbf{i}_{f,i} \|_2 \leq I_{i,\max}, \| \mathbf{i}_{g,i} \|_2 \leq I_{i,\max} \tag{12}$$

These constraints play a decisive role in transient behavior and stability under voltage sags or symmetrical faults.[19]

The continuous-time model is discretized for digital control implementation, yielding the general form in **Equation 13**. On this modeling basis, the control problem is formulated as tracking the nominal frequency $f_{\mathrm{nom}}$and nominal voltage V_{nom}, while reducing transients, ROCOF, oscillations, and control effort. The aggregated objective is written as in **Equation 14**, subject to the constraints $\mathbf{u}_k \in \mathcal{U}, \mathbf{x}_k \in \mathcal{X}, \mathbf{w}_k \in \mathcal{W}$.

$$\begin{aligned} \mathbf{x}_{k+1} &= \mathbf{x}_k + T_s \mathbf{f}\left(\mathbf{x}_k, \mathbf{u}_k, \mathbf{w}_k, \vartheta\right), \\ \mathbf{y}_k &= \mathbf{h}\left(\mathbf{x}_k\right) + \boldsymbol{\nu}_k \end{aligned} \tag{13}$$

$$\begin{aligned} \min_{\{\mathbf{u}_k\}} \mathcal{J} = \sum_{k=1}^{K} \big(& \alpha_\omega e^2_{\omega,k} + \alpha_V e^2_{V,k} \\ & + \alpha_\rho \rho_k^2 + \alpha_u \| \Delta \mathbf{u}_k \|_2^2 \big) \end{aligned} \tag{14}$$

where $\mathcal{J}$ denotes the scalar objective function minimized over the control sequence $\mathbf{u}_k$, representing the aggregated frequency error, voltage error, ROCOF, and control-input variation.

This formulation enables consistent comparison of robust control, MPC, and data-assisted variants on the same modeling platform and under the same hardware constraints.[44]

3. Theorem-like environments

This section describes three classes of control strategies for inverter-based microgrids, namely disturbance-oriented robust control, sliding-mode–based robust control, and constraint-aware predictive control. The formulation builds on the control-oriented model in **Section 2** and adopts a unified notation in which the aggregated state is denoted by $x \in \mathbb{R}^n$, the control input by $u \in \mathbb{R}^m$, the regulated output by $y \in \mathbb{R}^p$, and the lumped disturbance by w, representing RES variability, load steps, and measurement noise.

3.1. Active disturbance rejection control

In ADRC, parametric uncertainty and external disturbances are lumped into an equivalent disturbance channel and estimated online using an extended state observer. A generalized control-oriented representation of the disturbed system can be written as in **Equation 15**.[3]

$$\begin{aligned} \dot{x}\left(t\right) &= \mathcal{A}x\left(t\right) + \mathcal{B}u\left(t\right) + \mathcal{E}d\left(t\right), \\ y\left(t\right) &= \mathcal{C}x\left(t\right) \end{aligned} \tag{15}$$

where $x$is the state vector, $u$is the control input, $y$is the measured output, and $d$represents the lumped disturbance.

To explicitly incorporate disturbance estimation, an extended state $z$is introduced, leading to the augmented dynamics in **Equation 16**, which follow the standard ADRC framework.[3]

$$\begin{aligned} \dot{x}\left(t\right) &= \mathcal{A}x\left(t\right) + \mathcal{B}u\left(t\right) + \mathcal{G}z\left(t\right), \\ \dot{z}\left(t\right) &= \varphi\left(t\right), y\left(t\right) = \mathcal{C}x\left(t\right) \end{aligned} \tag{16}$$

An extended state observer is constructed to estimate both the system state and the lumped disturbance, as shown in **Equation 17**.[3]

$$\begin{aligned} & \dot{\hat{x}}\left(t\right) = \mathcal{A}\hat{x}\left(t\right) + \mathcal{B}u\left(t\right) \\ & + \mathcal{G}\hat{z}\left(t\right) + \mathcal{L}\left(y\left(t\right) - \hat{y}\left(t\right)\right), \\ & \dot{\hat{z}}\left(t\right) = \mathcal{L}_z\left(y\left(t\right) - \hat{y}\left(t\right)\right) \end{aligned} \tag{17}$$

with $\hat{y} = \mathcal{C}\hat{x}$, where $\mathcal{L}$and $\mathcal{L}_z$are observer gains.

Based on the disturbance estimate, the ADRC control law is expressed as in **Equation 18**,[3] where $u_0$is the nominal tracking controller and $\mathcal{K}\hat{z}$provides active disturbance compensation.

$$u\left(t\right) = u_0\left(t\right) - \mathcal{K}\hat{z}\left(t\right) \tag{18}$$

3.2. Sliding mode control with chattering mitigation

Sliding mode control addresses robustness by enforcing the system trajectory onto a predefined

sliding manifold. For frequency and voltage regulation, a composite sliding variable can be defined as in **Equation 19**, following classical and higher-order SMC formulations.

To reduce chattering while preserving robustness, a continuous boundary-layer approximation is commonly adopted, yielding the control law in **Equation 20**.[3,45]

$$\begin{aligned} s\left(t\right) &= e\left(t\right) + \mathcal{Q}\int_0^t e\left(\tau\right) d\tau, \\ e\left(t\right) &= y\left(t\right) - y^{\star}\left(t\right) \end{aligned} \tag{19}$$

$$u\left(t\right) = u_{\mathrm{eq}}\left(t\right) - \rho \mathrm{sat}\left(\frac{s\left(t\right)}{}\right) \tag{20}$$

where $u_{\mathrm{eq}}$is the equivalent control, $\rho$is the robustness gain, defines the boundary-layer thickness, and sat $(\cdot)$denotes the saturation function.

Such formulations have been extensively applied to inverter-based systems with LCL filters to achieve fast transient response under parameter uncertainty and load disturbances.[45]

3.3. Control model predictive control under constraints

Model predictive control formulates the regulation problem as a constrained optimization over a finite prediction horizon. Using the discretized control-oriented model, the predictive dynamics are written as in **Equation 21**.[46]

$$x_{k+1} = \mathcal{A}_d x_k + \mathcal{B}_d u_k + \mathcal{E}_d d_k, y_k = \mathcal{C}_d x_k \tag{21}$$

The multi-objective cost function for frequency–voltage tracking and control effort minimization over a horizon $N_p$is given by **Equation 22**.[47]

$$\begin{aligned} \min_{\mathbf{U}_k} Z_{\mathrm{MPC}} = \sum_{i=0}^{N_p-1} \left(y_{k+i} - y^{\star}_{k+i}{}^2_{\mathcal{W}_y} + u_{k+i}{}^2_{\mathcal{W}_u} \right) \\ + x_{k+N_p} - x^{\star}_{k+N_p}{}^2_{\mathcal{W}_f} \end{aligned} \tag{22}$$

where $U_k = [u_k^T, \ldots, u_{k+N_p-1}^T]^T$ is the predicted control sequence, and Z_{MPC} denotes the finite-horizon MPC objective function.

The optimization is subject to actuator and state constraints, as expressed in **Equation 23**.[46]

$$u_{\min} \le u_{k+i} \le u_{\max}, x_{\min} \le x_{k+i} \le x_{\max} \tag{23}$$

3.4. Lightweight machine learning augmentation

Lightweight ML methods are incorporated as auxiliary modules to provide fast estimation or approximation rather than replacing the core control structure. For extreme learning machines (ELMs), the regularized least-squares training problem can be written as in **Equation 24**,[48] where **H** is the hidden-layer activation matrix constructed from the measured signals, **r** is the learning target, such as the disturbance estimate or effective parameter, and λ is the regularization coefficient.

$$\begin{aligned} \hat{\theta} = \underset{\theta}{\mathrm{argmin}} \parallel \mathbf{H}\theta - \mathbf{r} \parallel_2^2 + \lambda \parallel \theta \parallel_2^2 \\ \Rightarrow \hat{\theta} = (\mathbf{H}^T\mathbf{H} + \lambda \mathbf{I})^{-1}\mathbf{H}^T\mathbf{r} \end{aligned} \tag{24}$$

For least squares support vector machine (LSSVM) regression, the kernel-based formulation is expressed as in **Equation 25**, following standard LSSVM theory,[20] where Z_{LSSVM} is the objective function of the LS-SVM problem, w is the weight vector, b is the bias term, ξ_i is the regression error, γ is the error-penalty coefficient, and the following condition describes the regression constraint between the target output r_i and the input feature $\phi(\zeta_i)$.

$$\begin{aligned} &\min_{w,b,\xi} \; Z_{\mathrm{LSSVM}} = \tfrac{1}{2}w_2^2 + \tfrac{\gamma}{2}\textstyle\sum_{i=1}^{N}\xi_i^2 \\ &\text{s.t.} \quad r_i = w^T\phi(\zeta_i) + b + \xi_i, \searrow i = 1, \ldots, N \end{aligned} \tag{25}$$

The ELM architecture employed as an auxiliary module is defined by a single hidden layer with $N_h$neurons, input $\mathrm{x} \in \mathbb{R}^d$, output $\mathrm{y} \in \mathbb{R}^m$, with mapping

$$\mathrm{y} = \mathrm{H}\left(\mathrm{x}\right)\beta, \mathrm{H}\left(\mathrm{x}\right) = \sigma\left(\mathrm{Wx} + \mathrm{b}\right), \tag{26}$$

where $\sigma\left(z\right) = \frac{1}{1+e^{-z}}$, $\mathrm{W} \in \mathbb{R}^{N_h \times d} \sim \mathcal{U}\left(\cdot\right)$, $\mathrm{b} \in \mathbb{R}^{N_h} \sim \mathcal{U}\left(\cdot\right)$(fixed), and only $\beta \in \mathbb{R}^{N_h \times m}$ is determined analytically via regularized least squares:

$$\beta = (\mathrm{H}^{\top}\mathrm{H} + \lambda \mathrm{I})^{-1}\mathrm{H}^{\top}\mathrm{Y}, \tag{27}$$

with H ∈ . Training reduces to a single pseudo-inversion of complexity $\mathcal{O}(N_h^2 N_s)$, while inference requires

$$\mathrm{y} = \mathrm{H}(\mathrm{x})\beta \Rightarrow \mathcal{O}(N_h), \tag{28}$$

hence it is non-iterative ("no backpropagation and no iterative optimization") and computationally lightweight.

The LSSVM model adopts the radial basis function kernel:

$$k(\mathrm{x}_i, \mathrm{x}_j) = \exp(-\gamma\|\mathrm{x}_i - \mathrm{x}_j\|^2), \gamma > 0, \tag{29}$$

with penalty parameter $C > 0$, selected via cross-validation. Instead of solving a quadratic programming problem with complexity $\mathcal{O}(N_s^3)$, training reduces to solving the linear system

$$\begin{bmatrix} 0 & 1^{\top} \\ 1 & \Omega + \frac{1}{C}\mathrm{I} \end{bmatrix} \begin{bmatrix} b \\ \alpha \end{bmatrix} = \begin{bmatrix} 0 \\ \mathrm{y} \end{bmatrix}, \tag{30}$$

where $\Omega_{ij} = k(\mathrm{x}_i, \mathrm{x}_j)$. The computational complexity is $\mathcal{O}(N_s^2 \log N_s)$. Inference is given by:

$$\hat{y}(\mathrm{x}) = \sum_{i=1}^{N_s} \alpha_i k(\mathrm{x}, \mathrm{x}_i) + b \Rightarrow \mathcal{O}(N_s). \tag{31}$$

Both ELM and LSSVM have low inference complexity and limited floating-point operation requirements, making them suitable as lightweight auxiliary modules for embedded inverter control under real-time implementation constraints.

In control applications, the learned output $\hat{d}(t)$or $\hat{f}(\mathrm{x})$is used as a disturbance estimate or surrogate model, for example: $u = u_{\mathrm{base}} + \hat{d}(t)$or $u = u(\hat{f}(\mathrm{x})$, providing low computational overhead while approximating nonlinear or unknown system components.

For ADRC–SMC integration, consider the disturbed system:

$$\dot{x} = f(x,t) + bu + d(t). \tag{32}$$

The extended state observer provides

$$\hat{d}(t) \approx d(t) + \Delta(t) \tag{33}$$

where L_o is the observer gain and bandwidth ω_o governs the trade-off: higher ω_o = faster estimation and increased noise sensitivity. SMC defines sliding surface $s(x) = 0$, control $u = u_{\mathrm{eq}} + u_{\mathrm{sw}}$, $u_{\mathrm{sw}} = -K\mathrm{sgn}(s)$, and $K \geq \|d(t)\|_\infty$; ensuring finite-time convergence $s \to 0$ but inducing chattering $\sim K$; hybridization yields $u = u_{\mathrm{eq}}(\hat{d}) + u_{\mathrm{sw}}$, residual disturbance $d_{\mathrm{res}} = d - \hat{d}$, hence $K \geq \|d_{\mathrm{res}}\|_\infty \ll \|d\|_\infty \Rightarrow$chattering $\downarrow$, robustness preserved.

Additionally, model-based feedforward $u_{\mathrm{ff}} = f_{\mathrm{nom}}(t; P_{\mathrm{load}}, P_{\mathrm{RES}})$ leads to composite control $u = u_{\mathrm{ff}} + u_{\mathrm{eq}}(\hat{d}) + u_{\mathrm{sw}}$, reducing feedback burden, pre-compensating predictable disturbances, and optimizing tracking, ROCOF attenuation, robustness, and computational efficiency within the real-time control loop.

4. Simulation and discussion

All controllers were evaluated under identical stochastic realizations per Monte Carlo run to ensure fair paired comparisons. Time was discretized as $t_k = k\Delta t$, with $\Delta t = 10^{-3}$s, total duration $T = 10$s, and $N = \mathrm{round}\,(T/\Delta t)$samples.

The normalized irradiance baseline was$g_{\mathrm{base}}\,(t) = 0.5 + 0.4\mathrm{sin}\,(2\pi \cdot 0.08t)\,, t \in [0,T]$, with two cloud events at $t_c \in \{3,7\}$ sapplied over $[t_c, t_c + 0.5)$by $g_{\mathrm{base}}\,(t) \leftarrow 0.3 g_{\mathrm{base}}\,(t)$.

For Monte Carlo run r, stochastic variability was injected as$g^{(r)}\,(t_k) = \max\left\{0,\ g_{\mathrm{base}}\,(t_k) + \sigma\,\xi_g^{(r)}\,(k)\right\}$, $\sigma = 0.03$, $\xi_g^{(r)}\,(k) \sim \mathcal{N}\,(0,1)$, and the PV power proxy follows the implemented scaling law $P_{\mathrm{pv}}^{(r)}\,(t_k) = 0.85\,g^{(r)}\,(t_k)$. The active-load baseline

$$P_{\ell,\mathrm{base}}\,(t) = 0.5 + 0.15\mathrm{sin}\,(2\pi \cdot 0.15t + \pi/4) + 0.1\mathrm{sin}\,(2\pi \cdot 0.3t) + 0.15\mathbb{I}_{(4,6)}\,(t) - 0.2\mathbb{I}_{(8,10)}\,(t)$$

and reactive-load baseline is

$$Q_{\ell,\mathrm{base}}\,(t) = 0.2 + 0.1\mathrm{sin}\,(2\pi \cdot 0.2t)\,.$$

Run-to-run uncertainty was injected as clipped Gaussian perturbations:

$$P_\ell^{(r)}\,(t_k) = \max\left\{0,\ P_{\ell,\mathrm{base}}\,(t_k) + \sigma\xi_P^{(r)}\,(k)\right\},$$

$$Q_\ell^{(r)}\,(t_k) = \max\left\{0,\ Q_{\ell,\mathrm{base}}\,(t_k) + \sigma\xi_Q^{(r)}\,(k)\right\}$$

with $\sigma = 0.03$and independent and identically distributed $\xi_P^{(r)}, \xi_Q^{(r)} \sim \mathcal{N}\,(0,1)$.

The study used $n_{\mathrm{runs}} = 5$Monte Carlo runs. Stochasticity arises from $\{\xi_g\,|\xi_P|\,\xi_Q\}$and lightweight ML initialization. In particular, ELM random weights/biases are generated with a run-index seed via $\mathrm{rng}\,(r)$, making the ML component deterministic per run. Full reproducibility was obtained by logging$\Delta t, T, n_{\mathrm{runs}}$and the RNG seed used at the start of the Monte Carlo loop, while keeping the per-run seeding convention for ML.

Let $f_k = f\,(t_k)$, $V_k = V\,(t_k)$, $f_{\mathrm{nom}} = 50Hz$, $V_{\mathrm{nom}} = 230\sqrt{2}$(peak), and define the frequency tracking error $e_k = f_k - f_{\mathrm{nom}}$.

Overshoot was computed directly on the trajectory

$\mathrm{OS}_f = \max_k f_k - f_{\mathrm{nom}}, \mathrm{US}_f = f_{\mathrm{nom}} - \min_k f_k$.Settling time is defined as the first index meeting the implemented band $\varepsilon_s = 0.02 f_{\mathrm{nom}}$(in Hz),$t_s = \min\{t_k :\ e_k < \varepsilon_s\}$,with $t_s = T$if the band is never reached. Rise time follows the 10–90% convention on the dominant excursion used in the code, i.e., $t_r = t_{90} - t_{10}$computed from the first crossings of $0.1\Delta f_{\max}$and $0.9\Delta f_{\max}$. Voltage deviation was evaluated in root-mean-square form $V_{k,\mathrm{rms}} = V_k/\sqrt{2}$as:

$$\Delta V_{\max} = \max_k \frac{V_{k,\mathrm{rms}} - V_{\mathrm{nom}}/\sqrt{2}}{V_{\mathrm{nom}}/\sqrt{2}}. \tag{34}$$

Peak frequency deviation and ROCOF were quantified as:

$$\Delta f_{\max} = \max_k e_k, \mathrm{ROCOF}_{\max} = \max_k \frac{f_{k+1} - f_k}{\Delta t} \tag{35}$$

Robustness to stochastic RES/load perturbations is summarized over Monte Carlo runs $r = 1, \ldots, n_{\mathrm{runs}}$via mean and a Student-$t$ confidence interval:

$$\bar{m} = \frac{1}{n_{\mathrm{runs}}} \sum_{r=1}^{n_{\mathrm{runs}}} m^{(r)}, \mathrm{CI}_{1-\alpha} = t_{1-\alpha/2,\ n_{\mathrm{runs}}-1} \frac{s_m}{\sqrt{n_{\mathrm{runs}}}} \tag{36}$$

Table 1. Frequency tracking and dynamic performance metrics.

Algorithm	RMSE (Hz)	IAE (Hz·s)	ROCOF (Hz/s)
ADRC	0.008049 ± 0.001631	0.065903 ± 0.012241	0.344849 ± 0.009233
SMC	0.009115 ± 0.000029	0.086233 ± 0.000293	0.350189 ± 0.006176
ELM	0.009844 ± 0.000018	0.077119 ± 0.000190	0.114441 ± 0.004737
LSSVM	0.009134 ± 0.000023	0.069748 ± 0.000194	0.111389 ± 0.006176
MPC	0.074881 ± 0.000211	0.616180 ± 0.001316	0.165558 ± 0.002594
Fuzzy-PID	0.007530 ± 0.000010	0.055856 ± 0.000108	0.115967 ± 0.002594

Abbreviations: ADRC: Active disturbance rejection control; ELM: Extreme learning machine; IAE: Integral absolute error; LSSVM: Least squares support vector machine; MPC: Model predictive control; PID: Proportional integral derivative; RMSE: Root mean square error; ROCOF: Rate of change of frequency; SMC: Sliding mode control.

where s_m is the sample standard deviation across runs.

Let the implemented control proxy be $u_k = P_{c,k}$. Control effort and control ripple are captured by:

$$J_u = \frac{1}{N}\sum_{k=1}^{N} u_k, \sigma_u^2 = \mathrm{var}\left(u_k\right). \tag{37}$$

For waveform-quality assessment, total harmonic distortion (THD) is computed on the quasi-steady window $t \in [5, 5.5)$using detrended signals $V_{\mathrm{win}}$and the power-consistent current proxy $I_k = \frac{P_{\mathrm{pv}}(t_k) - P_\ell(t_k) + P_c(t_k)}{V_{k,\mathrm{rms}}}$, with harmonic magnitudes $\{V_h\}_{h\geq 1}$and $\{I_h\}_{h\geq 1}$obtained from the discrete spectrum,

$$\mathrm{THD}_v = \frac{\sqrt{\sum_{h=2}^{H} V_h^2}}{V_1}, \mathrm{THD}_i = \frac{\sqrt{\sum_{h=2}^{H} I_h^2}}{I_1}$$

If true voltage–current waveforms (including phase transformation) are available, a compatible extension is the fundamental power factor $\mathrm{PF}_1 = P_1/\left(V_1 I_1\right)$; otherwise, THD and control-effort statistics provide the primary signal-quality surrogates.

Table 1 summarizes three core metrics for frequency-tracking performance evaluation. Fuzzy- proportional–integral–derivative (PID) achieves the best frequency tracking (root mean square error [RMSE] = 0.00753 ± 0.00001 Hz; integral absolute error [IAE] = 0.05586 ± 0.00011 Hz·s), representing the lowest values among the six algorithms and indicating effective error suppression over the full simulation horizon. ADRC ranks second (RMSE = 0.00805 ± 0.00163 Hz; IAE = 0.06590 ± 0.01224 Hz·s). MPC yields the largest tracking errors (RMSE = 0.07488 ± 0.00021 Hz; IAE = 0.61618 ± 0.00132 Hz·s), indicating limited disturbance rejection under the current configuration. ROCOF exhibits a different ordering. LSSVM achieves the lowest ROCOF (0.11139 ± 0.00618 Hz/s), followed by ELM (0.11444 ± 0.00474 Hz/s) and Fuzzy-PID (0.11597 ± 0.00259 Hz/s). ADRC and SMC exhibit the highest ROCOF (0.345–0.350 Hz/s).

The ROCOF values reported in **Table 1** reveal a structural distinction among the six evaluated strategies, which can be interpreted through the control law $u(t)$and the induced frequency derivative $\frac{df}{dt}$. ADRC and SMC produce the largest ROCOF (0.345–0.350 Hz/s). For ADRC, the control law in **Equation 18** has the form $u = u_0 - \hat{d}(t)/b$, where $\hat{d}(t) \approx d(t)$, implying $\Delta u \propto -\hat{d}(t) \Rightarrow \frac{df}{dt}$ increase immediately after disturbance. For SMC (**Equation 20**), $u = u_{\mathrm{eq}} - \rho \mathrm{sgn}(s)$, $\dot{s} = -\rho \mathrm{sgn}(s) \Rightarrow s(t) \to 0$ in finite time $T \leq \frac{|s(0)|}{\rho}$, hence large $\rho \Rightarrow |\ \frac{df}{dt}\ |$. Under a load step ΔP, both yield impulsive-like correction $u(t) \sim \delta(t)$in effect, producing large transient $\frac{df}{dt}$before settling.

Mitigation in ADRC corresponds to reducing observer bandwidth $\omega_o \downarrow \Rightarrow \hat{d}(t) \to d(t)$slower, or filtering $u_d = \mathcal{F}(s)\hat{d}(t)$ with rate limit $|\ \frac{du}{dt}\ | \leq r_{\max}$, yielding lower ROCOF but higher $\|e(t)\|$. In SMC, reducing ρ or replacing $\mathrm{sgn}(s)$by $\mathrm{sat}(s/\phi)$gives $u_{\mathrm{sw}} = -\rho \mathrm{sat}(s/\phi) \Rightarrow |\ \frac{df}{dt}\ | \downarrow$ but weakens the robustness condition $\rho \geq \|d(t)\|_\infty$.

For MPC, the moderate value $ROCOF \approx 0.166 Hz/s$ follows from the optimization in **Equation 22**: $\min_{u_{k:k+N-1}} \sum_{i=0}^{N-1} \left(\|x_{k+i} - x^\star\|_Q^2 + \|u_{k+i}\|_R^2\right)$, subject to $x_{k+i+1} = f(x_{k+i}, u_{k+i})$, implying distributed correction u_{k+i}over horizon $N \Rightarrow \frac{df}{dt}$bounded and smooth; however, limited bandwidth $\omega_c \sim \frac{1}{NT_s} \Rightarrow$larger tracking error with $\mathrm{RMSE} = 0.07488$ Hz, $\mathrm{IAE} = 0.61618$ Hz. Improvement requires tuning N, weights Q/R, and disturbance model $d_{k+i|k}$, i.e. $(N, Q, R, \hat{d}) \mapsto \min\{\mathrm{ROCOF}, \mathrm{RMSE}, \mathrm{IAE}\}$.

These results show ROCOF $\equiv /f(\mathrm{tracking})$ but is structurally linked to

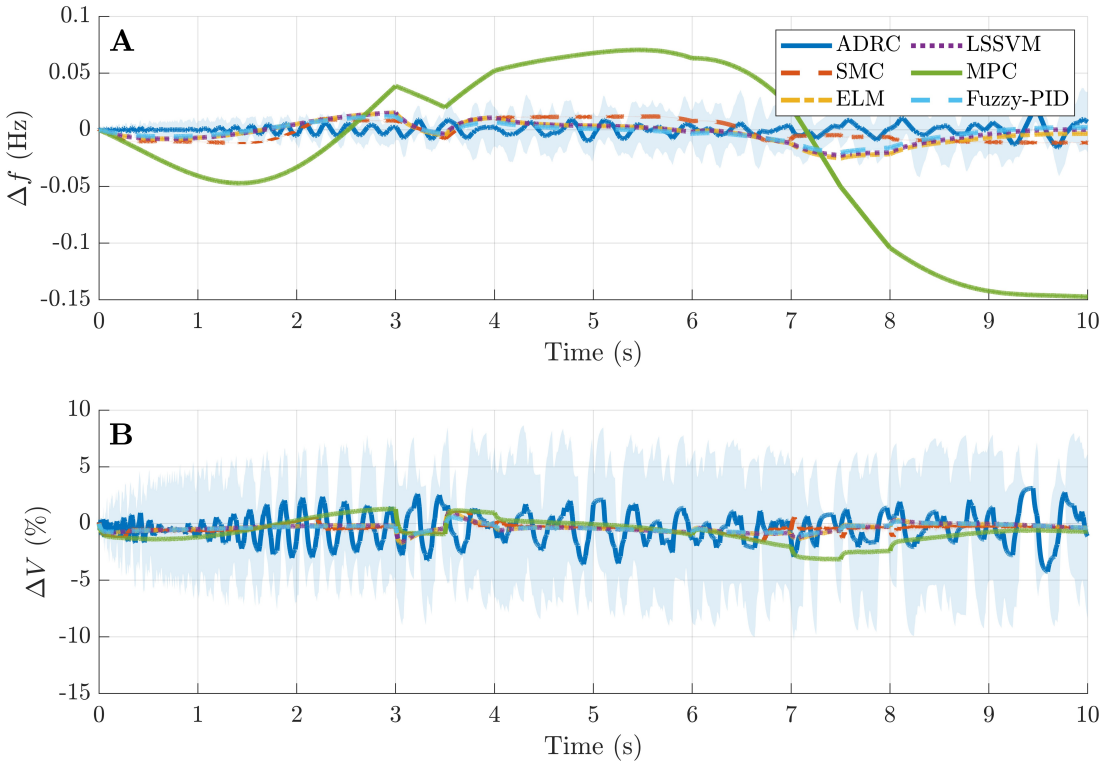

Figure 1. Time-domain frequency and voltage regulation responses under identical stochastic operating scenarios. (A) Frequency and (B) voltage deviations.

control action distribution $u(t)$in time: impulsive $u(t) \Rightarrow| \frac{df}{dt} |\uparrow$, distributed $u(t) \Rightarrow| \frac{df}{dt} |\downarrow$. Therefore, controller synthesis should include ROCOF explicitly, such as constraint $| \frac{df}{dt} | \leq ?_{max}(Hz/s)$ or penalty $J = J_{\text{track}} + \lambda \int \left(\frac{df}{dt}\right)^2 dt$, instead of indirect tuning

Figure 1 presents the frequency Δf(t) and voltage ΔV(t) trajectories for the six algorithms, including 95% confidence intervals. MPC exhibits a pronounced drift and sustained deviation, which becomes clearly evident after approximately 7 s. Fuzzy-PID achieves the lowest mean voltage deviation ΔV_{mean}. ADRC shows more pronounced oscillations and a wider confidence band.

Figure 2 shows the activity level of the control signal over time after smoothing. MPC exhibits the flattest control signal, with small amplitude variation and limited oscillation. Smooth control does not imply good tracking. MPC still produces the largest RMSE and IAE in **Table 1** and yields the largest maximum frequency deviation Δf_{max} as presented in **Table 2**. This pattern indicates that the current MPC configuration prioritizes control magnitude reduction rather than fast disturbance rejection. Horizon length, weights, and constraint handling likely govern this outcome. ADRC and SMC show stronger control variations, which align with their larger ROCOF in **Table 1** and are consistent with overshoot and undershoot levels in **Table 3**. The trade-off between fast tracking and smooth actuation is evident.

Figure 3 presents RMSE and IAE with uncertainty visualization. Fuzzy-PID performs best in terms of RMSE and IAE. MPC is an outlier in the unfavorable direction. RMSE and IAE are approximately one order of magnitude larger than those of the other controllers. The gap indicates a systematic property of the current MPC configuration under the simulated scenario.

Table 2 adds extreme value and waveform quality metrics. The maximum frequency deviation (MaxDF_{mean}) is largest for MPC at 0.14739 Hz, whereas the remaining algorithms range from 0.012 to 0.025 Hz. Mean voltage deviation (ΔV_{mean}) is smallest for Fuzzy-PID at 0.01260 p.u., which corresponds to about 1.26%. The largest value is ADRC at 0.06420 p.u., which corresponds to about 6.42%. A common interpretive reference for voltage magnitude at the point of common coupling is around 10% under normal conditions, and all mean deviations remain within this envelope. The remaining differentiators relate to ripple and harmonic content.

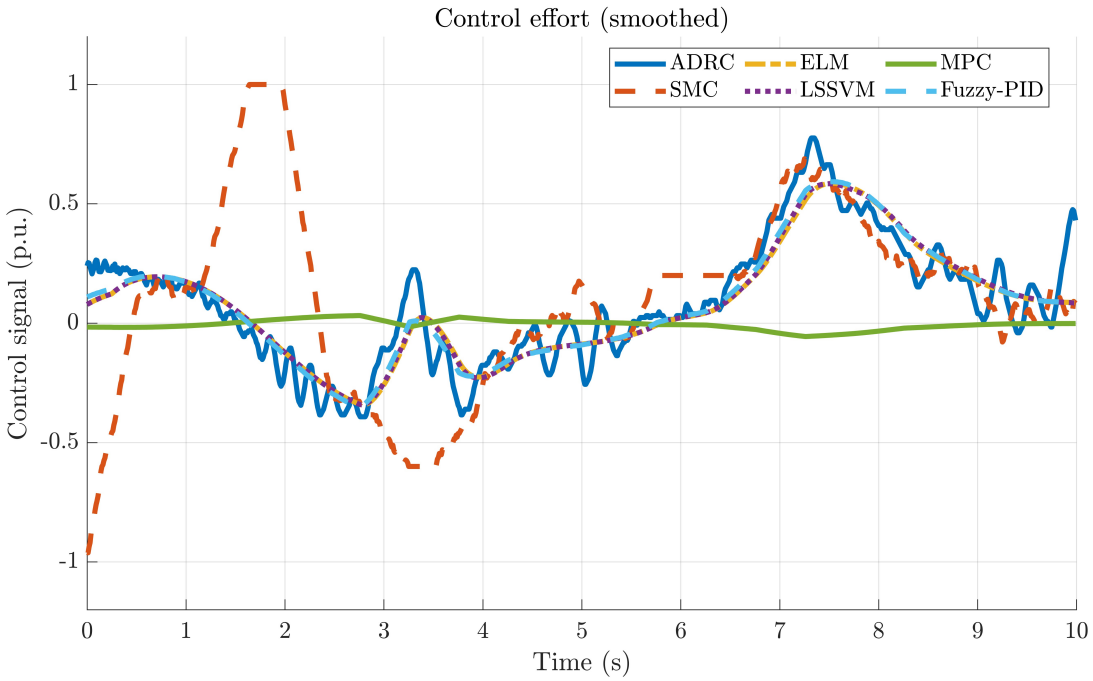

Figure 2. Smoothed control signal responses of the evaluated controllers.

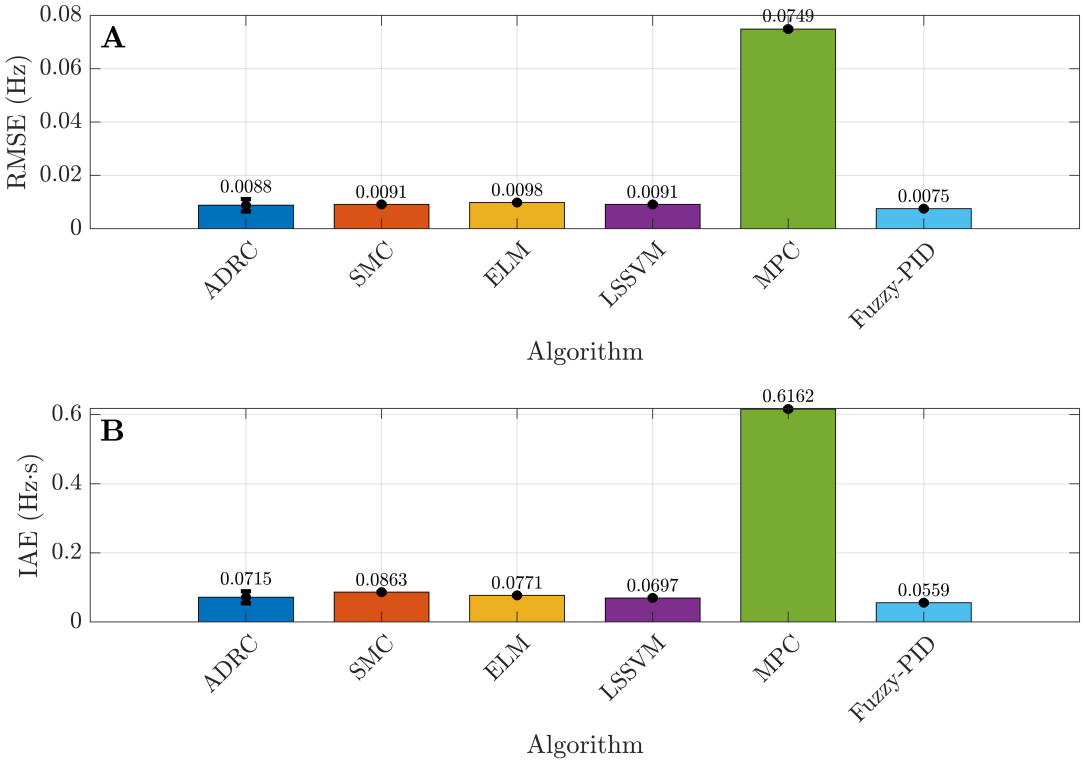

Figure 3. Statistical comparison of RMSE and IAE frequency tracking metrics. (A) RMSE and (B) IAE with uncertainty bands.

These aspects are reflected by power spectral density (PSD) and THD results. Voltage THD ($THDv_{mean}$) is 3.295% for SMC, while the other algorithms cluster between 5.1% and 5.65%. ADRC reaches 11.593%, which exceeds the 5% reference limit. This outcome implies a strong risk

Table 2. Power quality metrics for frequency, voltage, and harmonics

Algorithm	Δf_max (Hz)	ΔV (p.u.)	THD_v (%)	THD_i (%)
ADRC	0.019706 ± 0.003713	0.064202 ± 0.001699	11.5928 ± 12.1769	4.0054 ± 3.8791
SMC	0.012007 ± 0.000070	0.016340 ± 0.000288	3.2951 ± 1.6445	9.3548 ± 6.9217
ELM	0.025137 ± 0.000080	0.017296 ± 0.000302	5.1151 ± 3.7954	12.4118 ± 0.2084
LSSVM	0.022720 ± 0.000104	0.016421 ± 0.000289	5.1176 ± 3.8138	12.5441 ± 0.3590
MPC	0.147392 ± 0.000598	0.031907 ± 0.000091	5.1709 ± 4.0936	14.6546 ± 3.9972
Fuzzy-PID	0.020021 ± 0.000044	0.012600 ± 0.000198	5.6485 ± 3.3631	10.6379 ± 7.1792

Abbreviations: Δf_max: Maximum frequency deviation; ΔV: Voltage deviation; THD_i: Total harmonic distortion of current; THD_v: Total harmonic distortion of voltage.

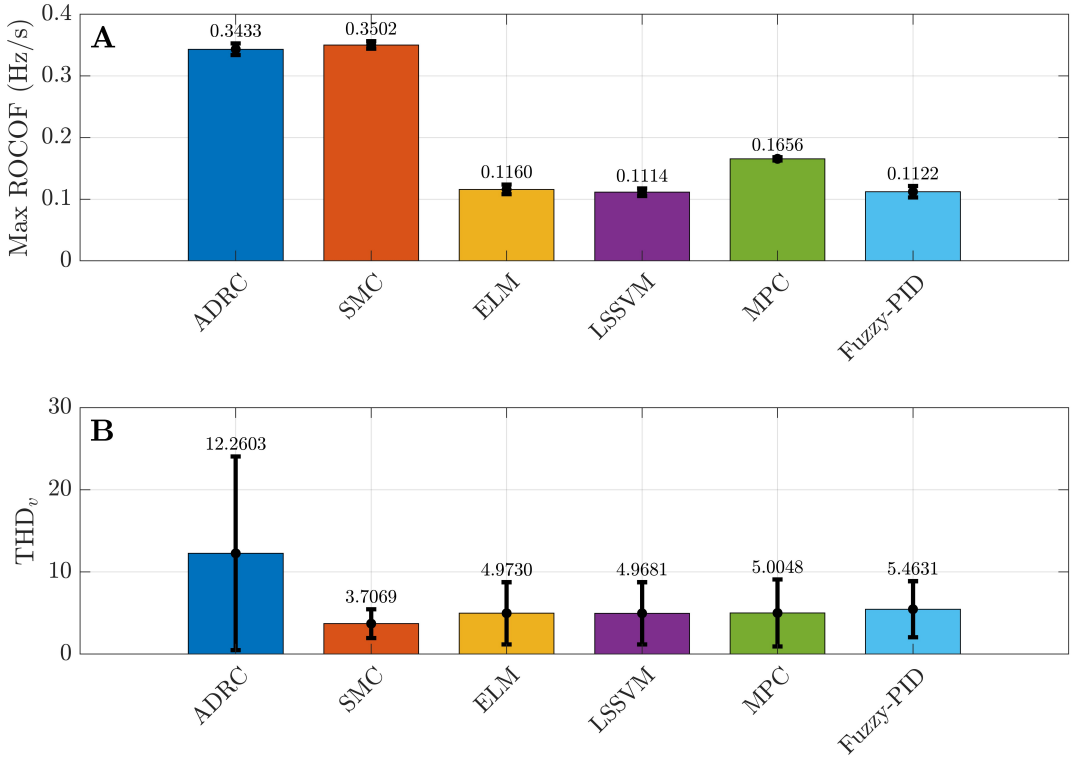

Figure 4. Comparison of maximum ROCOF and voltage total harmonic distortion across controllers. (A) ROCOF and (B) THDv comparison.

of noncompliance in voltage harmonic quality if the measurement is interpreted at the point of common coupling.

Figure 4 highlights the trade-off between frequency dynamics and harmonic quality. ROCOF is smallest for LSSVM, ELM, and Fuzzy-PID, indicating a softer frequency response. THDv is smallest for SMC, indicating superior voltage harmonic performance under the chosen metric. ADRC combines high ROCOF with high THDv, suggesting strong actuation with substantial voltage distortion. This combination indicates the need for harmonic mitigation measures.

Table 3 characterizes control intensity and transient overshoot behavior. MPC yields CtrlEff_{mean} of 0.017063, the smallest among the algorithms, and CtrlVar_{mean} of 0.000463, also the smallest. Additionally, Overshoot_{mean} is 0.0704. ADRC yields CtrlEff_{mean} of approximately 0.999 and CtrlVar_{mean} of approximately 0.993, indicating intense actuation. Overshoot and undershoot are about 0.0197 and 0.0196, respectively. Fuzzy-PID yields CtrlEff_{mean} of approximately 0.200, representing a moderate level. The algorithm achieves the best tracking (**Table 1**) and the smallest ΔV_{mean} (**Table 2**). This pattern indicates a favorable trade-off between tracking,

Table 3. Control activity and overshoot metrics

Algorithm	Control effort (p.u.)	Control variance	Overshoot (Hz)	Undershoot (Hz)
ADRC	0.999278 ± 0.000244	0.993348 ± 0.000823	0.019693 ± 0.003737	0.019595 ± 0.003642
SMC	0.957524 ± 0.000971	0.938639 ± 0.001380	0.012007 ± 0.000070	0.011945 ± 0.000041
ELM	0.192824 ± 0.000424	0.055186 ± 0.000157	0.014922 ± 0.000087	0.025137 ± 0.000080
LSSVM	0.194944 ± 0.000469	0.056083 ± 0.000164	0.014911 ± 0.000085	0.022720 ± 0.000104
MPC	0.017063 ± 0.000043	0.000463 ± 0.000001	0.070400 ± 0.000492	0.147392 ± 0.000598
Fuzzy-PID	0.200236 ± 0.000458	0.059085 ± 0.000164	0.011950 ± 0.000043	0.020021 ± 0.000044

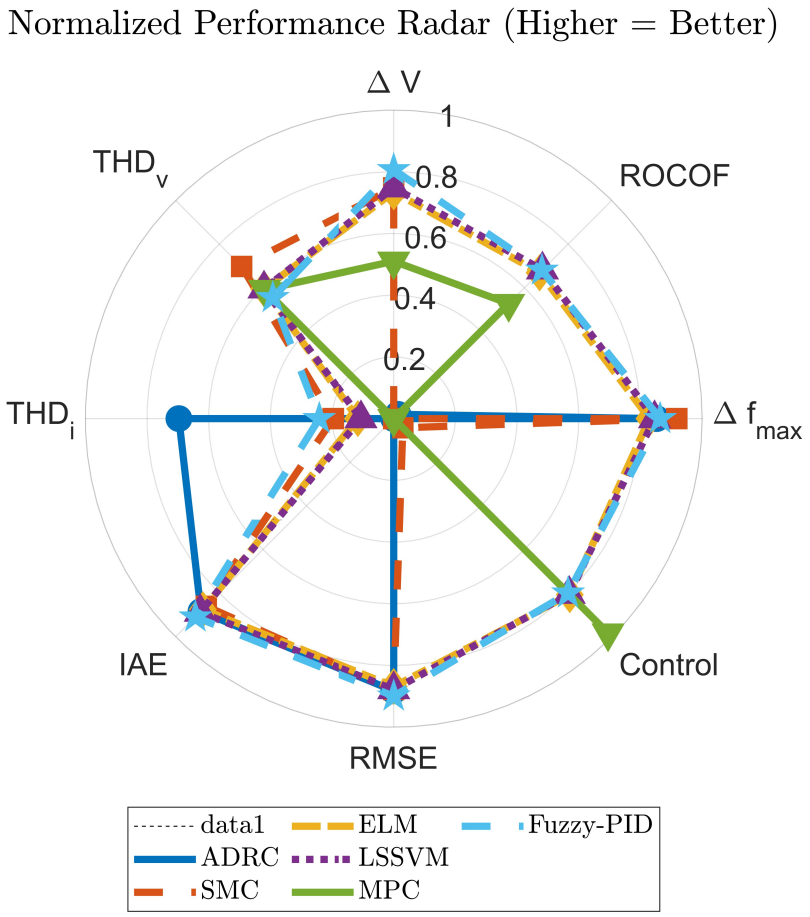

Figure 5. Normalized radar chart of multi-criteria controller performance.

control effort, and mean voltage deviation under the current configuration.

Figure 5 summarizes multi-criteria behavior: Fuzzy-PID stands out along the tracking-related axes (RMSE and IAE) and along the voltage deviation axis (ΔV). SMC stands out along THDv, while MPC stands out along the control axis. MPC performs poorly along RMSE, IAE, and Δf_{max}.

Figure 6 reports normalized scores across metric groups (RMSE, IAE, control, and THD). Fuzzy-PID yields the lowest overall score, driven by its dominance in RMSE and IAE and its low ΔV. MPC yields the highest overall score, with penalties from RMSE, IAE, and Δf_{max} dominating the total.

Figure 7 presents the trade-off structure across metrics. MPC sits low on the control axis but high on RMSE, IAE, and Δf_{max}, indicating smooth control with poor tracking. Fuzzy-PID sits low on RMSE and IAE, and its moderate control effort and THD, indicating strong track-

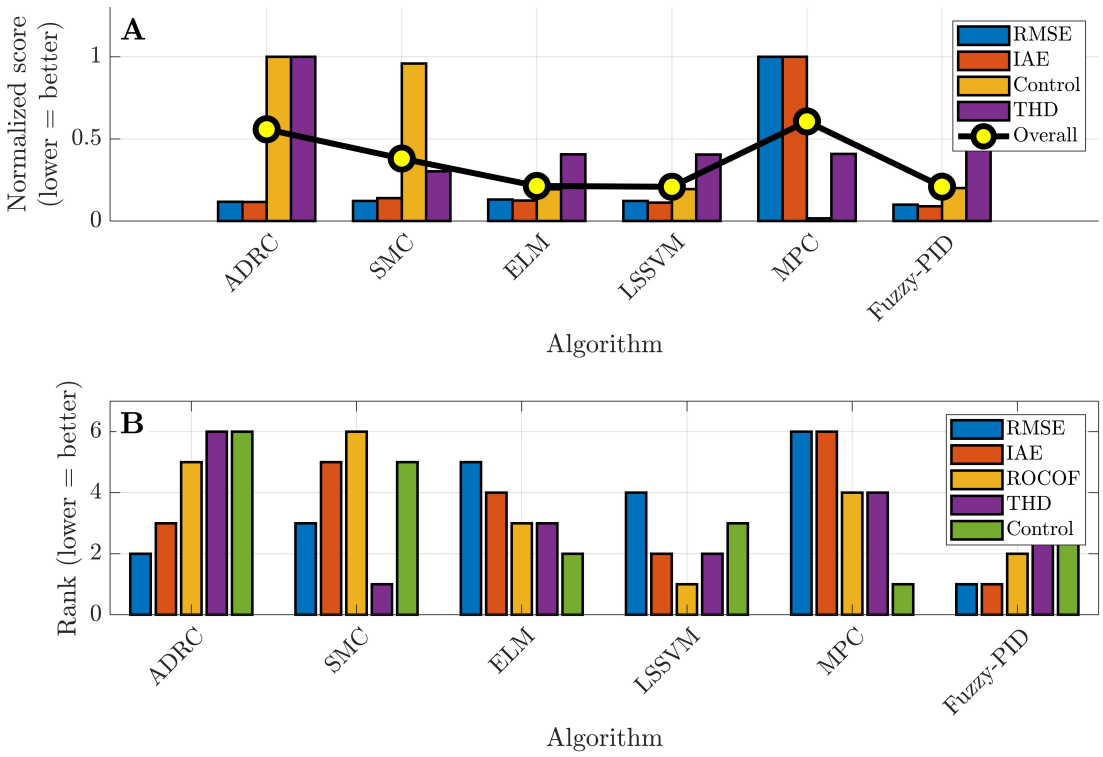

Figure 6. Multi-criteria performance aggregation and metric-wise ranking of the evaluated controllers. (A) Multi-criteria performance comparison. (B) Ranking across metrics.

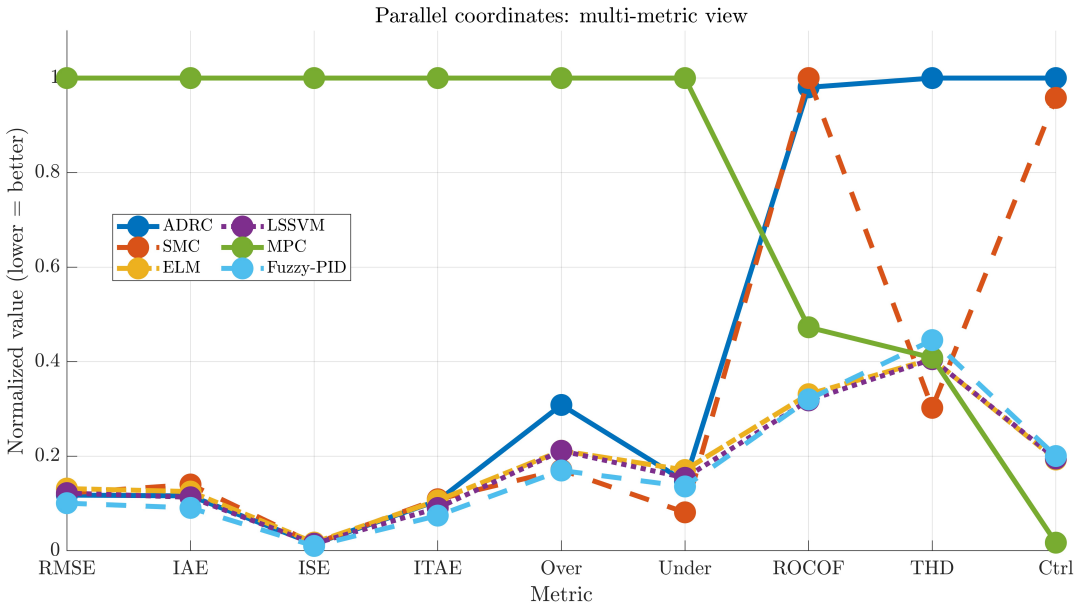

Figure 7. Parallel-coordinate visualization of normalized multi-metric controller performance.

ing with harmonic performance that still requires improvement. SMC sits low on THD but remains moderate to high on integral error measures, indicating clean voltage harmonics with suboptimal tracking performance.

Figure 8 shows transient responses under cloud and load step windows. The cloud transient window shows MPC with a clear increasing trend in Δf, while other algorithms remain closer to 0. The load step window shows SMC with

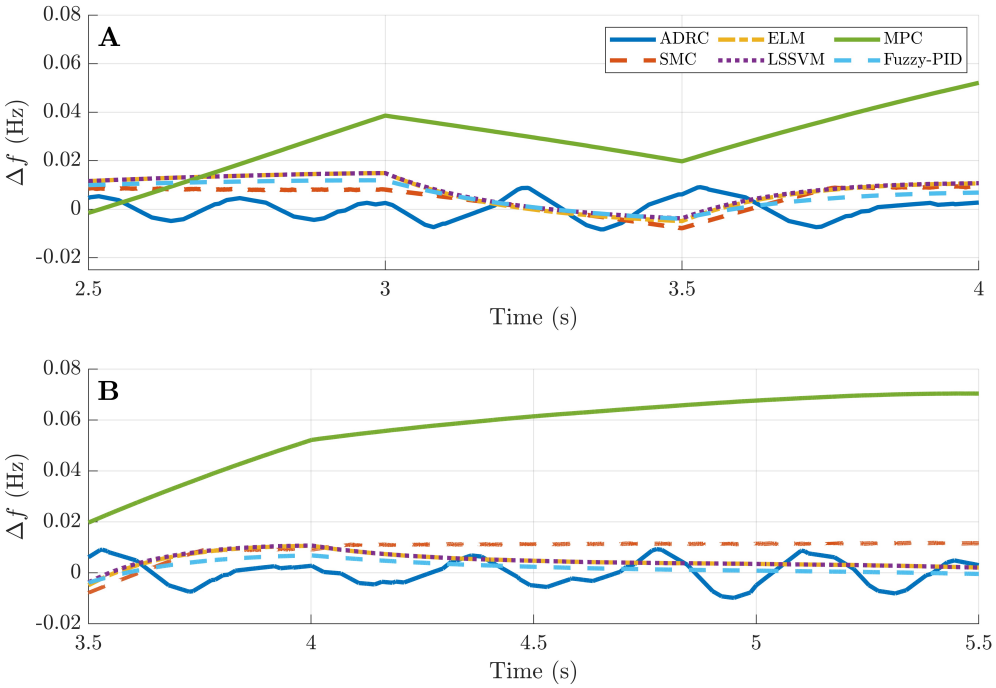

Figure 8. Event-driven transient frequency responses under renewable and load disturbances. (A) Cloud transient response. (B) Load step response.

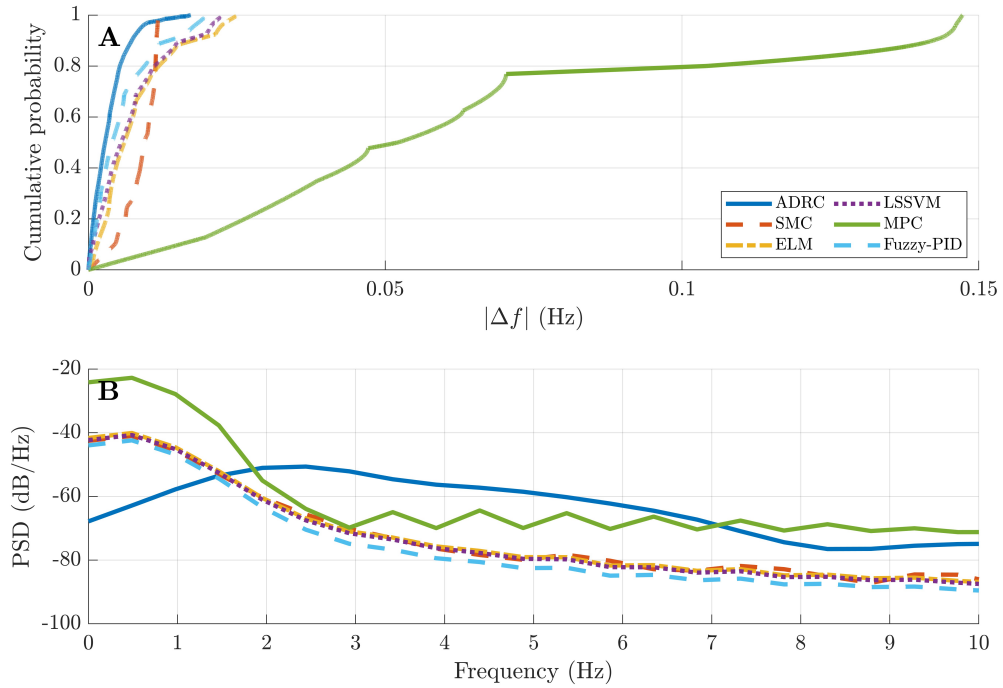

Figure 9. Statistical and spectral characterization of frequency tracking error. (A) Cumulative distribution function of absolute frequency error. (B) Power spectral density.

a more persistent positive Δf offset. Fuzzy-PID shows a softer response with smaller excursions, while LSSVM and ELM exhibit similar behavior. **Figure 8** supports the conclusion that the current MPC configuration is not well-suited for fast disturbances and power variability in the sim-

ulated scenario. The lightweight learning-based controllers, ELM and LSSVM, yield low ROCOF and smoother responses.

Figure 9 presents the cumulative distribution function of absolute frequency error $|\Delta f|$ and the power spectral density PSD. The cumulative distribution function curve of Fuzzy-PID rises faster in the small $|\Delta f|$ region, indicating a higher probability of small errors. This behavior matches the best RMSE and IAE. MPC exhibits a long tail up to about 0.15 Hz, indicating more frequent large errors. The PSD comparison shows more prominent low-frequency spectral energy for MPC and ADRC in certain bands, suggesting slow drift or prolonged transients. ELM, LSSVM, Fuzzy-PID, and SMC exhibit stronger spectral decay toward higher frequencies, indicating fewer fast oscillatory components.

In summary, Fuzzy-PID achieves the best frequency tracking quality with an RMSE of 0.00753 Hz and an IAE of 0.05586 Hz·s. Additionally, it achieves the smallest mean voltage deviation, with ΔV_{mean} of 0.01260 p.u. The algorithm leads the overall ranking. SMC is the strongest option for voltage harmonic quality with THDv of 3.295%. MPC yields the smoothest and smallest control action with CtrlEff_{mean} of 0.01706, but this comes at the cost of significantly degraded tracking performance, with RMSE of 0.07488 Hz and IAE of 0.61618 Hz·s. MPC also yields a high Δf_max and ranks last under the current configuration. ROCOF values show that LSSVM, ELM, and Fuzzy PID provide softer frequency dynamics, reducing frequency stress under low inertia operation. Mean voltage deviation magnitudes remain well below the approximately 10% reference envelopes often discussed under the EN 50160 framework. The main differentiators across algorithms arise from harmonic distortion and transient dynamics rather than mean voltage deviation magnitude.

5. Conclusion

This study presents a controlled and reproducible comparison of six frequency and voltage control strategies for inverter-dominated microgrids under identical experimental scenarios, simulation settings, and stochastic disturbances. By fixing renewable generation profiles, load step events, measurement noise levels, and Monte Carlo seeds, the evaluation isolated the intrinsic performance characteristics of each controller without confounding effects from scenario design, enabling a consistent basis for cross-method comparison across time-domain, spectral, and statistical performance indicators.

From a quantitative standpoint, Fuzzy-PID control delivered the most balanced performance across the evaluated metrics, achieving the lowest frequency tracking errors with RMSE of 0.00753 Hz and IAE of 0.05586 Hz·s, together with the smallest mean voltage deviation of 0.0126 p.u. SMC demonstrated superior voltage harmonic quality, reducing voltage THD to 3.30%, but exhibited higher ROCOF values around 0.35 Hz/s, indicating increased dynamic stress. Lightweight learning-assisted controllers based on ELM and LSSVM achieved low ROCOF values near 0.11 Hz/s, indicating smoother frequency dynamics, although their tracking accuracy remained inferior to Fuzzy-PID control. MPC showed the lowest control activity, with a mean control effort of 0.017 p.u. and minimal control variance, confirming its ability to generate smooth actuation signals. However, this benefit came at the expense of poor disturbance rejection, reflected by the largest frequency tracking errors and maximum frequency deviations among all tested methods.

These findings indicate that controller selection in inverter-dominated microgrids must be guided by explicit operational priorities, such as tracking accuracy, harmonic quality, or actuation smoothness. Future work should extend this framework toward adaptive weighting of performance metrics, hardware-in-the-loop validation, and hybrid architectures that combine robust control structures with lightweight data-driven modules to improve performance while preserving real-time feasibility and reproducibility.

Acknowledgments

The author gratefully acknowledges the support of Thai Nguyen University of Technology and the Education Technology and Adaptive Learning Institute, Thai Nguyen University of Technology, Vietnam.

Funding

None.

Conflict of interest

The author declares no conflicts of interest in this work.

Author contributions

This is a single-authored article.

Availability of data

Data are available from the corresponding author upon reasonable request.

AI tools statement

The author confirms that no AI tools were used in the preparation of this manuscript.

References

1. Musca R, Vasile A, Zizzo G. Grid-forming converters. A critical review of pilot projects and demonstrators. *Renewable and Sustainable Energy Reviews*. 2022;165:112551. https://www.doi.org/10.1016/j.rser.2022.112551
2. Teng Y, Deng W, Pei W, et al. Review on grid-forming converter control methods in high-proportion renewable energy power systems. *Global Energy Interconnection*. 2022;5(3):328-342. https://www.doi.org/10.1016/j.gloei.2022.06.010.
3. Rathnayake DB, Akrami M, Phurailatpam C, et al. Grid Forming Inverter Modeling, Control, and Applications. *IEEE Access*. 2021;9:114781-114807. https://www.doi.org/10.1109/ACCESS.2021.3104617
4. Gu Y, Green TC. Power System Stability With a High Penetration of Inverter-Based Resources. *Proc IEEE*. 2023;111(7):832-853. https://www.doi.org/10.1109/jproc.2022.3179826
5. Sajadi A, Kenyon RW, Hodge BM. Synchronization in electric power networks with inherent heterogeneity up to 100% inverter-based renewable generation. *Nat Commun*. 2022;13(1). https://www.doi.org/10.1038/s41467-022-30164-3
6. Cheema KM. A comprehensive review of virtual synchronous generator. *International Journal of Electrical Power & Energy Systems*. 2020;120:106006. https://www.doi.org/10.1016/j.ijepes.2020.106006
7. Kannan A, Nuschke M, Dobrin BP, et al. Frequency stability analysis for inverter dominated grids during system split. *Electric Power Systems Research*. 2020;188:106550. https://www.doi.org/10.1016/j.epsr.2020.106550
8. He X, Huang L, Subotić I, et al. Quantitative Stability Conditions for Grid-Forming Converters With Complex Droop Control. *IEEE Trans Power Electron*. 2024;39(9):10834-10852. https://www.doi.org/10.1109/TPEL.2024.3404251
9. Zhang H, Yu S, Xiong L, et al. Power instruction correction based frequency response strategy for grid forming inverter in islanded microgrids. *International Journal of Electrical Power & Energy Systems*. 2024;155:109551. https://www.doi.org/10.1016/j.ijepes.2023.109551
10. Ordono A, Sanchez-Ruiz A, Zubiaga M, et al. Current limiting strategies for grid forming inverters under low voltage ride through. *Renewable and Sustainable Energy Reviews*. 2024;202:114657. https://www.doi.org/10.1016/j.rser.2024.114657
11. Abudyak YH, Rezaei MH, Abdelnabi AAB, et al. Grid-Forming Inverters Review: Control, Stability, and the Next Stage With Artificial Intelligence and Digital Twins. *IEEE Open J Power Electron*. 2026;7:351-387. https://www.doi.org/10.1109/OJPEL.2026.3654526
12. IEEE Standard for Interconnection and Interoperability of Inverter-Based Resources Interconnecting with Associated Transmission Electric Power Systems. https://www.doi.org/10.1109/IEEESTD.2022.9762253
13. Elbouchikhi E, El Moubarek AB, Abouloifa A, et al. Active disturbance rejection control for four-wire inverters in standalone renewable resources-based microgrid — islanded microgrids ADRC-based control. *ISA Transactions*. 2025;156:290-306. https://www.doi.org/10.1016/j.isatra.2024.11.006
14. Li J, You H, Liu S, et al. Active disturbance rejection distributed secondary control for DC microgrids. *High Voltage*. 2024;9(1):241-251. https://www.doi.org/10.1049/hve2.12398
15. Liu S, You H, Li J, et al. Active disturbance rejection control based distributed secondary control for a low-voltage DC microgrid. *Sustainable Energy, Grids and Networks*. 2021;27:100515. https://www.doi.org/10.1016/j.segan.2021.100515
16. Ning B, Han QL, Ding L. Distributed Secondary Control of AC Microgrids With External Disturbances and Directed Communication Topologies: A Full-Order Sliding-Mode Approach. *IEEE/CAA J Autom Sinica*. 2021;8(3):554-564. https://www.doi.org/10.1109/JAS.2020.1003315
17. Wu L, Liu J, Vazquez S, et al. Sliding Mode Control in Power Converters and Drives: A Review. *IEEE/CAA J Autom Sinica*. 2022;9(3):392-406. https://www.doi.org/10.1109/JAS.2021.1004380
18. Rosero CX, Rosero F, Tapia F. Fully Decentralized Sliding Mode Control for Frequency Regulation and Power Sharing in Islanded Microgrids. Energies. 2025;18(20):5495. https://www.doi.org/10.3390/en18205495
19. Qi X, Zheng J, Mei F. Model Predictive Control–Based Load-Frequency Regulation of Grid-Forming Inverter–Based Power Systems. *Front Energy Res*. 2022;10. https://www.doi.org/10.3389/fenrg.2022.932788

20. Ullah Q, Costa Resende E, Carlos Gomes Freitas L, et al. Enhancing voltage stability of grid forming power converters based on model predictive controller. *International Journal of Electrical Power & Energy Systems*. 2024;163:110317. https://www.doi.org/10.1016/j.ijepes.2024.110317
21. Heydari R, Young H, Flores-Bahamonde F, et al. Model-Free Predictive Control of Grid-Forming Inverters With LCL Filters. *IEEE Trans Power Electron*. 2022;37(8):9200-9211. https://www.doi.org/10.1109/TPEL.2022.3159730
22. Meng J, Zhang Z, Zhang G, et al. Adaptive model predictive control for grid-forming converters to achieve smooth transition from islanded to grid-connected mode. *IET Generation Trans & Dist*. 2023;17(12):2833-2845. https://www.doi.org/10.1049/gtd2.12859
23. Dangeti LSN, Marimuthu R. Distributed model predictive control strategy for microgrid frequency regulation. *Energy Reports*. 2025;13:1158-1170. https://www.doi.org/10.1016/j.egyr.2024.12.071
24. Lin Y, Zhu J, He F, et al. A Data-Driven Model-Free Predictive Voltage Control Strategy for Grid-Forming Inverters. *IEEJ Transactions Elec Engng*. 2025;20(12):2045-2052. https://www.doi.org/10.1002/tee.70078
25. Al Kez D, Foley AM, Ahmed F, et al. Overview of frequency control techniques in power systems with high inverter-based resources: Challenges and mitigation measures. *IET Smart Grid*. 2023;6(5):447-469. https://www.doi.org/10.1049/stg2.12117
26. Khan M, Wu W, Li L. Grid-forming control for inverter-based resources in power systems: A review on its operation, system stability, and prospective. *IET Renewable Power Gen*. 2024;18(6):887-907. https://www.doi.org/10.1049/rpg2.12991
27. Shahgholian G, Moradian M, Fathollahi A. Droop control strategy in inverter-based microgrids: A brief review on analysis and application in islanded mode of operation. *IET Renewable Power Gen*. 2025;19(1). https://www.doi.org/10.1049/rpg2.13186
28. Mohammed N, Ali M, Ciobotaru M, et al. Accurate control of virtual oscillator-controlled islanded AC microgrids. *Electric Power Systems Research*. 2023;214:108791. https://www.doi.org/10.1016/j.epsr.2022.108791
29. Sowa I, Tran TT, Heins T, et al. An Average Consensus Algorithm for Seamless Synchronization of Andronov-Hopf Oscillator Based Multi-Bus Microgrids. *IEEE Access*. 2021;9:90441-90454. https://www.doi.org/10.1109/ACCESS.2021.3090657
30. Zhao Q, Han Z, Wang S, et al. Coordinated control of multiple converters in model-free AC/DC distribution networks based on reinforcement learning. *Front Energy Res*. 2023;11. https://www.doi.org/10.3389/fenrg.2023.1202701
31. Xing L, Shu Z, Fang J, et al. Distributed control of DC microgrids: A relaxed upper bound for constant power loads. *Automatica*. 2025;173:112021. https://www.doi.org/10.1016/j.automatica.2024.112021
32. Said SM, Aly M, Hartmann B, et al. Coordinated fuzzy logic-based virtual inertia controller and frequency relay scheme for reliable operation of low-inertia power system. *IET Renewable Power Gen*. 2021;15(6):1286-1300. https://www.doi.org/10.1049/rpg2.12106
33. Wang X, Li J, Guo Q, et al. Parameter Design of Half-Bridge Converter Series Y-Connection Microgrid Grid-Connected Filter Based on Improved PSO-LSSVM. Singh AR, ed. *International Transactions on Electrical Energy Systems*. 2023;2023:1-13. https://www.doi.org/10.1155/2023/9534004
34. Kondaiah VY, Saravanan B, Sanjeevikumar P, et al. A review on short-term load forecasting models for micro-grid application. *The Journal of Engineering*. 2022;2022(7):665-689. https://www.doi.org/10.1049/tje2.12151
35. Xing X, Jia L. Energy management in microgrid and multi-microgrid. *IET Renewable Power Gen*. 2023;18(15):3480-3508. https://www.doi.org/10.1049/rpg2.12816
36. Chen R, Xu H, Zhou L, et al. Underfrequency Load Shedding Strategy With an Adaptive Variation Capability for Multi-Microgrids. *IEEE Access*. 2023;11:17294-17304. https://www.doi.org/10.1109/ACCESS.2023.3246088
37. Rodriguez-Martinez OF, Andrade F, Vega-Penagos CA, et al. A Review of Distributed Secondary Control Architectures in Islanded-Inverter-Based Microgrids. *Energies*. 2023;16(2):878. https://www.doi.org/10.3390/en16020878
38. Hezzi A, Elbouchikhi E, Bouzid A, et al. Active Disturbance Rejection Control for Distributed Energy Resources in Microgrids. *Machines*. 2024;12(1):67. https://www.doi.org/10.3390/machines12010067
39. Akinwola AB, Alkuhayli A. Walrus Optimization-Based Adaptive Virtual Inertia Control for Frequency Regulation in Islanded Microgrids. *Electronics*. 2025;14(20):3980. https://www.doi.org/10.3390/electronics14203980
40. Elkasem Ahmed HA, Kamel S, Hassan MH, et al. An Eagle Strategy Arithmetic Optimization Algorithm for Frequency Stability Enhancement Considering High Renewable Power Penetration and Time-Varying Load. *Mathematics*. 2022;10(6):854.

https://www.doi.org/10.3390/math10060854
41. Rosso R, Wang X, Liserre M, et al. Grid-Forming Converters: Control Approaches, Grid-Synchronization, and Future Trends—A Review. *IEEE Open J Ind Applicat.* 2021;2:93-109. https://www.doi.org/10.1109/OJIA.2021.3074028
42. Chen WH, Yang J, Guo L, et al. Disturbance-Observer-Based Control and Related Methods—An Overview. *IEEE Trans Ind Electron.* 2016;63(2):1083-1095. https://www.doi.org/10.1109/TIE.2015.2478397
43. Sufyan A, Jamil M, Ghafoor S, et al. A Robust Nonlinear Sliding Mode Controller for a Three-Phase Grid-Connected Inverter with an LCL Filter. *Energies.* 2022;15(24):9428. https://www.doi.org/10.3390/en15249428
44. Huang GB, Zhu QY, Siew CK. Extreme learning machine: Theory and applications. *Neurocomputing.* 2006;70(1-3):489-501. https://www.doi.org/10.1016/j.neucom.2005.12.126
45. Espín-Sarzosa D, Palma-Behnke R, Cañizares CA, et al. Microgrid Modeling for Stability Analysis. *IEEE Trans Smart Grid.* 2024;15(3):2459-2479. https://www.doi.org/10.1109/TSG.2023.3326063
46. Paspatis AG, Konstantopoulos GC, Dedeoglu S. Control design and small-Signal stability analysis of inverter-Based microgrids with inherent current limitation under extreme load conditions. *Electric Power Systems Research.* 2021;193:106929. https://www.doi.org/10.1016/j.epsr.2020.106929
47. Rogalla S, Ernst P, Lens H, et al. Grid-forming converters in interconnected power systems: Requirements, testing aspects, and system impact. *IET Renewable Power Gen.* 2024;18(15):3053-3066. https://www.doi.org/10.1049/rpg2.12967
48. Baeckeland N, Chatterjee D, Lu M, et al. Overcurrent Limiting in Grid-Forming Inverters: A Comprehensive Review and Discussion. *IEEE Trans Power Electron.* 2024;39(11):14493-14517. https://www.doi.org/10.1109/TPEL.2024.3430316

Minh-Cuong Nguyen *received his Ph.D. degree in Electrical Engineering from the Graduate University of Science and Technology, Vietnam Academy of Science and Technology (VAST), in 2021. He is currently a lecturer in the Department of Electric Power Systems, Thai Nguyen University of Technology (TNUT), Vietnam, and serves as the Director of the Education Technology and Adaptive Learning Institute at TNUT. His research interests include the optimization of energy systems, distributed generation, distribution systems in deregulated electricity markets, and renewable energy. He also focuses on optimal and nonlinear control, renewable energy integration, and the application of intelligent techniques in distributed power grid control.*

https://orcid.org/0009-0000-7543-8937